Available online at www.sciencedirect.com
ScienceDirect
Trans. Nonferrous Met. Soc. China 35(2025) 3074−3092
Transactions of Nonferrous Metals Society of China
www.tnmsc.cn

Preparation of porous α-Ga_2O_3 nanowires by dealloying of Ga-based liquid metals to enhance cycling stability for lithium storage

Chang LUO[1#], Zi-gang WANG[1#], Yi-chao WANG[2], Shuai-ju MENG[3], Hui YU[1], Wei-min ZHAO[1], Chun-ling QIN[1], Zhi-feng WANG[1]

1. "The Belt and Road Initiative" Advanced Materials International Joint Research Center of Hebei Province, School of Materials Science and Engineering, Hebei University of Technology, Tianjin 300401, China;
2. School of Science, RMIT University, Melbourne VIC 3001, Australia;
3. State Key Laboratory of Advanced Processing and Recycling of Nonferrous Metals, Lanzhou University of Technology, Lanzhou 730050, China

Received 5 January 2024; accepted 2 September 2024

Abstract: Ga_2O_3 is considered a potential anode material for next-generation lithium-ion batteries due to its high theoretical capacity and unique self-healing capability. To develop a novel preparation method and in-depth understanding of the electrochemical reaction mechanism of Ga_2O_3, a brand-new liquid−liquid dealloying strategy was exploited to construct porous α-Ga_2O_3 nanowire networks. Profiting from the well-designed porous structure, the material exhibits impressive cycling stability of a reversible capacity of 603.9 mA·h/g after 200 cycles at 1000 mA/g and a capacity retention of 125.2 mA·h/g after 100 cycles at 0.5C when assembling to Ga_2O_3//$LiFePO_4$ full cells. The lithiation/delithiation reaction mechanism of the porous Ga_2O_3 anodes is further revealed by ex-situ Raman, XRD, TEM measurements, and density functional theoretical (DFT) calculations, which establishes a correlation between the electrochemical performance and the phase transition from α-Ga_2O_3 to β-Ga_2O_3 during cycling.
Key words: liquid metal dealloying; porous nanowires; Ga_2O_3; Li-ion battery; anode

1 Introduction

Over the past few decades, the market of portable electronics, electric vehicles, and large-scale renewable energy storage units has been captured by lithium-ion batteries (LIBs) [1−3]. However, there still remains the urgent task of the development of next-generation LIBs with higher power density, longer terms of cycle life and competitive costs, to fight the ever-growing energy demands [4,5]. It is significantly critical to explore an ideal alternative anode material for the commercialized graphite anode, to achieve an improvement in the electrochemical performance of the LIBs [6−8]. Among the potential candidates, gallium (Ga) has attracted enormous attention owing to its relatively high theoretical capacity (769 mA·h/g), low melting point of 29.8 °C (possesses self-healing properties to avoid structural collapse and pulverization), and fascinating chemo-physical properties [9,10]. However, originating from the low surface energy of Ga liquid, the Ga nanoparticles tend to aggregate during cycling, leading to unsatisfactory cycling stability [11,12]. In this situation, pure Ga anodes confront significant challenges in the path to actual implementation.

[#] Chang LUO and Zi-gang WANG contributed equally to this work
Corresponding author: Zhi-feng WANG, Tel: +86-22-60202006, E-mail: wangzf@hebut.edu.cn
https://doi.org/10.1016/S1003-6326(25)66867-1

Instead of the pure Ga anodes, it seems to be capable of fabricating the solid Ga-based compounds (e.g., $CuGa_2$, GaN, and Ga_2O_3) as the anode materials [12,13]. Among various Ga-based compounds, Ga_2O_3 has been in the spotlight as the promising anode material for the next-generation LIBs due to the following advantages: (1) Ga_2O_3 suffers the typical conversion and alloying reaction during cycling, such a multiple reaction mechanism can effectively alleviate the severe volume change of electrode materials; (2) the lithiation/delithiation product of Ga metal presents a self-healing effect to prevent the electrode from structurally collapsing during cycling; (3) compared to traditional transition metal oxides, the relatively low average operating potential of Ga_2O_3-based anodes can provide a higher working potential when assembled to full cells; (4) Ga_2O_3 can provide a high theoretical capacity of 1430 mA·h/g, which is nearly four times that of commercialized graphite anodes [14−16].

In recent years, considerable efforts have been made to develop high-performance Ga_2O_3-based anodes and explore their reaction mechanism. To improve the electrical conductivity and ion/electron transport kinetics of Ga_2O_3 electrodes, conductive agents including amorphous carbon, graphene, and reduced graphene oxide (rGO) have been introduced and they have been demonstrated to be a practical method of achieving outstanding cycling stability [16−19]. In addition, based on different thermodynamic stability among various phases of Ga_2O_3, PATIL et al [20] proposed a novel strategy to control phase composition by regulating the content of hybridized rGO in Ga_2O_3/rGO anodes, and studied the variations in lithium storage capability. These efforts made a major contribution to the advancement of Ga_2O_3-based anodes. Although significant progress has been made, novel preparation methods for Ga_2O_3 anodes and an in-depth understanding of the electrochemical reaction mechanism of Ga_2O_3 are still needed.

Herein, porous α-Ga_2O_3 nanowires were fabricated through a first-developed liquid−liquid dealloying approach (dealloying of Ga-based liquid metals in liquid corrosion solution). α-Ga_2O_3 nanowires with different phase compositions were tailored and their Li storage performance was evaluated. The capacity fading mechanism of the electrode was revealed through ex-situ Raman, XRD, and TEM tests. The as-developed liquid−liquid dealloying strategy is of great significance for further development of dealloying technology and the preparation and exploitation of novel nanostructured materials.

2 Experimental

2.1 Fabrication of AgSn, Ag and Sn ribbons

The fabrication of AgSn ribbons contains electric arc melting and melt spinning, which was described in the previous work [21]. In a typical process, alloy ingots with a nominal composition of $Ag_{20}Sn_{80}$ were prepared under an argon atmosphere by arc-melting of high-purity Ag and Sn (99.99 wt.%) ingots. For the melt spinning process, the as-obtained ingot was remelted by induction melting and the melts were immediately ejected under pressure differential onto a water-cooled copper roller with a rotating speed of ~2400 r/min. In this way, the AgSn ribbons with 25 μm in thickness, 2−3 mm in width, and several centimeters in length were successfully fabricated. Pure Ag and Sn ribbons were also prepared via a similar route and the same experimental parameters.

2.2 Fabrication of GaOOH powders

The GaOOH powders were fabricated by a liquid−liquid dealloying process. Firstly, the as-prepared $Ag_{20}Sn_{80}$ ribbons (2 g) were immersed in the Ga liquid metal (3 mL) at 75 °C for 24 h to form the uniform Ga−Ag−Sn liquid metal. The dealloying process was activated by adding a proper content of 5 wt.% NaOH solution into the liquid metal at 75 °C and the reaction lasted for 36 h. During the free-leaching process, there was a clear observation of the GaOOH (denoted as GaOOH−AgSn) powders that emerged in the beaker. At the end of the dealloying process, the formed GaOOH powders were separated from the liquid system and then centrifuged several times by NaOH solution, ultra-pure water (18.25 MΩ·cm), and absolute ethanol, respectively. Before the following experimental steps, the collected GaOOH powders were dried at 60 °C for 12 h in a vacuum oven. For comparison purposes, GaOOH powders were also prepared by using the pure Ag and Sn ribbons (denoted as GaOOH−Ag and GaOOH−Sn), respectively.

2.3 Fabrication of porous Ga_2O_3 nanowires

To obtain the porous Ga_2O_3, the as-prepared GaOOH−AgSn powders were calcined with a heating rate of 5 °C/min at various temperatures: 450 °C (denoted as Ga_2O_3-450), 700 °C (denoted as Ga_2O_3-700) and 900 °C (denoted as Ga_2O_3-900). The calcination process lasted for 2 h [20]. In addition, the Ga_2O_3−Ag and Ga_2O_3−Sn were also obtained by calcining GaOOH−Ag and GaOOH−Sn at 450 °C for 2 h, respectively.

2.4 Materials characterization

The morphology and structure of the samples were observed by a scanning electron microscope (SEM, Quanta 450 FEG) and a transmission electron microscope (TEM, JEOL JEM 2100F) which was equipped with an X-ray energy dispersive spectroscope (EDS, OXDORD X-Max 80). Phase compositions were determined by an X-ray diffractometer (XRD, Bruker, D8) with Cu K_α radiation. The nitrogen adsorption and desorption isotherm was measured by an ASAP 2010 M+C analyzer. The Brunauer−Emmett−Teller (BET) method and Barrett−Joyner−Halenda (BJH) method were utilized to calculate the specific surface area and pore size distribution of the products, respectively. The valence states of the surface elements were established by an X-ray photoelectron spectroscope (XPS, ESCALAB 250). Raman spectra were examined at 532 nm (LabRAM HR Evolution).

2.5 Electrochemical performance measurements

CR 2032 coin-type half cells were assembled in a glove box filled with argon protection to measure the electrochemical performance. For the preparation of the electrode, the active materials (Ga_2O_3 powders), conductive additives (ketjen black), and binder (carboxymethyl cellulose) were mixed with a mass ratio of 7∶2∶1. The mixed powders were dissolved in ultrapure water to form a uniform slurry and then pasted on a copper foil. The electrodes were subsequently dried at 60 °C for 12 h. The mass loading of the active materials is 1.0−1.1 mg/cm^2. The adopted electrolyte consists of 1 mol/L $LiPF_6$ in ethylene carbonate/diethyl carbonate (EC/DEC volume ratio of 1∶1). Lithium disks and the Celgard 2400 were used as the counter electrode and separator, respectively. The mass loading of electrolyte was optimized to 60 μL/cell. Galvanostatic charge and discharge testing was carried out through a battery testing system (NEWARE, CT−4000) in the potential window of 0.01−3 V (vs Li^+/Li) at ambient temperature. Cyclic voltammetry (CV) profiles were recorded by a Princeton VersaSATA−4 electrochemical working station at a scan rate of 0.1 mV/s in the potential range of 0.01−3 V (vs Li/Li^+). The EIS curves were measured in a frequency range from 10 mHz to 100 kHz.

2.6 Full cells assembly and tests

The cathodes were prepared by mixing commercial $LiFePO_4$ powder, super P, and poly-vinylidene difuoride (PVDF) in a mass ratio of 8∶1∶1 and then dispersed in N-methylpyrrodone solution to form a uniform slurry. The resulting slurry was subsequently coated on the carbon-modified aluminum foil. Eventually, the working cathodes were created by punching the dried Al foils into disks with a diameter of 10 mm. The anode-to-cathode (N/P) capacity ratio was set up to be between 1.05 and 1.1. Galvanostatic charge and discharge measurements of the full cells were carried out in a potential range of 0.5−4 V (vs Li/Li^+) under ambient temperature. All the chemical sources used in this study, as well as the theoretical calculation methods, are presented in Supporting Information (SI).

3 Results and discussion

3.1 Structure characteristics

Figure 1 illustrates the overall fabrication route of the porous Ga_2O_3 nanowires. In the initial preparation step, the uniform Ga−Ag−Sn liquid alloy precursor was obtained through the low-temperature alloying process, which enables alloying of liquid Ga with other metals without the limitation of high temperature [22]. Figures S1(a) and (b) in SI show the XRD patterns of $Ag_{20}Sn_{80}$ precursor ribbons at 25 °C and liquid Ga−Ag−Sn alloy at 75 °C, respectively. It can be known that the $Ag_{20}Sn_{80}$ ribbons contain Sn phase (JCPDS No. 86-2265) and Ag_3Sn phase (JCPDS No. 71-0530), whereas liquid Ga-based phase (JCPDS No. 26-0666) and Ag_3Ga phase (JCPDS No. 47-0991) are detected in the liquid Ga−Ag−Sn alloy at the experimental temperature, demonstrating the feasibility of the above low-temperature alloying strategy. The dealloying reaction was awakened by

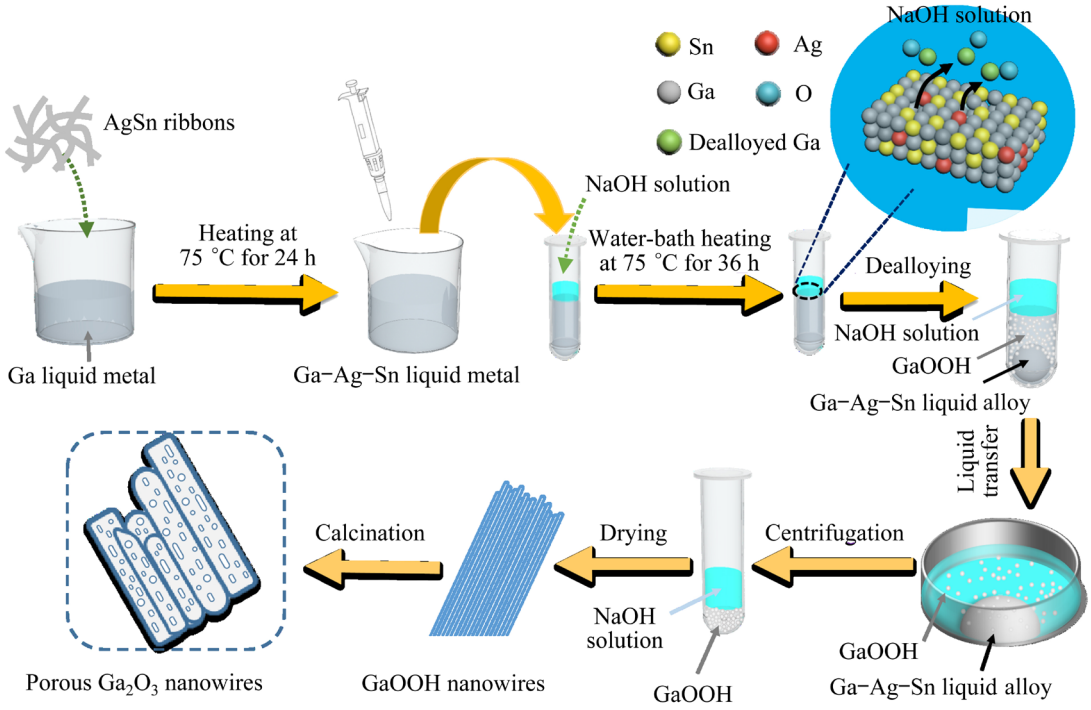

Fig. 1 Schematic illustration of synthesis process of porous Ga_2O_3 nanowires

the introduction of NaOH solution. In this liquid−liquid dealloying process, Ga in Ga−Ag−Sn liquid alloy was selectively removed, and then, the dissolved Ga reacted with the oxygen in the corrosive liquid. The related reaction can be depicted as the following reaction:

$$4Ga+2H_2O+3O_2=4GaOOH \quad (1)$$

According to previous studies [23], two key parameters reveal an important effect on the dealloying reaction kinetics, which include electrochemical potential differences between different components in the precursor alloy, and the diffusivity of noble elements at the precursor alloy/dealloying etchant interface. In this work, the introduced Ag−Sn ribbons are responsible for producing remarkable electrochemical potential differences between Ag/Sn and Ga in the Ga−Ag−Sn alloy and tuning the diffusivity of noble atoms at the liquid−liquid (Ga−Ag−Sn/NaOH) interface, resulting in the enhanced dealloying reaction kinetics.

As shown in Fig. S2(a) and Fig. S3(a) in SI, there was no reaction activity while immersing the pure Ga liquid into the NaOH solution. The surface of the Ga liquid remained smooth and shiny even underwent 36 h. Meanwhile, the immersed Ga−Ag, Ga−Sn, and Ga−Ag−Sn liquid alloys presented a grey surface with obvious powders embedded on the liquid metal surface (Figs. S2(b−d) and Figs. S3(b−d) in SI). The observed slow reaction kinetics of the pure Ga system might be related to the passivated liquid−liquid interface (Fig. 2), which will interrupt the constant consumption of Ga ions. In contrast, the dealloying reaction would rapidly proceed at the liquid−liquid (Ga−Ag−Sn/NaOH) interface, and selective and continuous etching of Ga from Ga−Ag−Sn liquid alloys (Ga presents the lowest corrosion potential in the constituent elements), owing to the enhanced dealloying reaction kinetics. In this case, GaOOH powders were obtained in the Ga−Ag, Ga−Sn, and Ga−Ag−Sn liquid systems (insets in Figs. S2(b−d) in SI), while there was no product produced in the pure Ga liquid metal (Fig. S2(a) in SI). Interestingly, the residual Ga−Ag−Sn liquid alloy that has been passivated can be recycled by repeating the low-temperature alloying process after the dealloying procedure terminated spontaneously, and it can further be utilized as the precursor of the liquid−liquid dealloying strategy mentioned above.

The main differences between the conventional solid−liquid dealloying and the as-developed liquid−liquid dealloying can be described below.

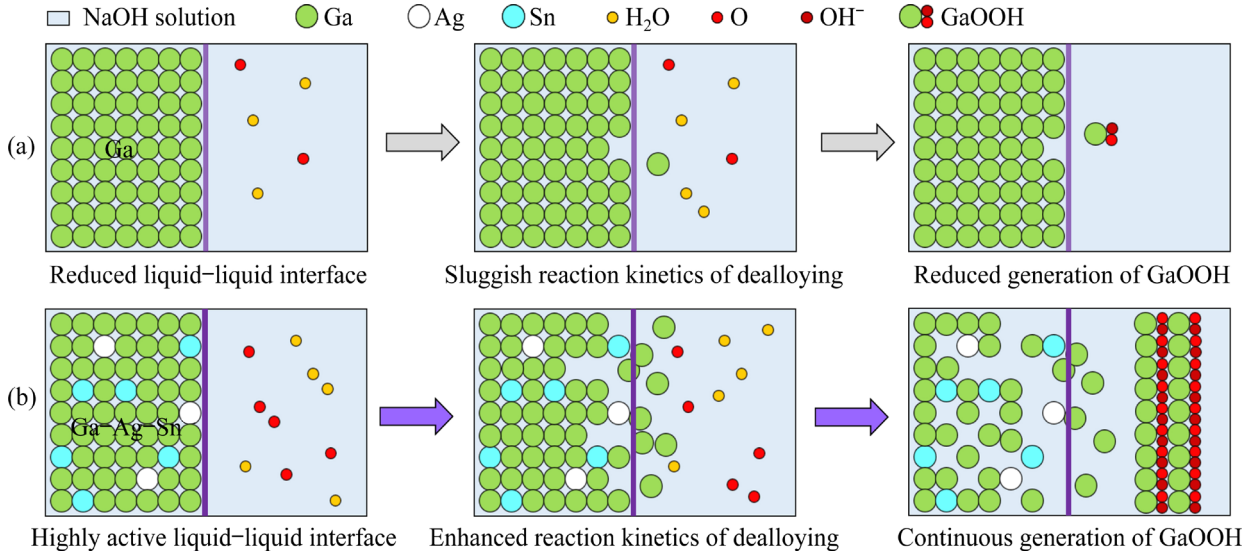

Fig. 2 Schematic illustration of reaction mechanism of pure Ga liquid metal (a) and Ga−Ag−Sn liquid alloy (b)

Firstly, the state of the material to be etched is different. In the conventional solid−liquid dealloying process, solid materials are etched, while in the liquid−liquid dealloying process, liquid alloys are etched. Secondly, dealloying occurs at different locations. During the conventional solid−liquid dealloying process, the etching liquid enters the inside of the solid material and etches in the three-dimensional space. During the liquid−liquid dealloying process, etching occurs at the interface of liquid metal and corrosive liquid. Thirdly, the dealloying products are different. The product of conventional solid−liquid dealloying is the relatively precious metal in the alloy, while the precious metal component remains in the liquid metal during liquid−liquid dealloying, and the non-precious metal reacts with the corrosive liquid to form the product at the interface. The liquid−liquid dealloying strategy has the potential to be extended to synthesize other new-type nano-structured materials by selecting various liquid metals and corrosion solutions.

The composition and crystal structure of the dealloyed products were determined by XRD. The XRD patterns of GaOOH−AgSn, GaOOH−Ag and GaOOH−Sn are presented in Fig. S4(a) in SI. Obviously, the three samples are characterized by similar Bragg diffraction peak positions. The sharp diffraction peaks located at 2θ values of 21.5°, 26.7°, 33.7°, 35.3°, 37.2°, 54.0° and 60.0° are related to (110), (120), (130), (021), (111), (221) and (151) crystal planes of GaOOH (JCPDS No. 54-0910), respectively, confirming the successful fabrication of the GaOOH [24]. The XRD results suggest the feasibility of obtaining the GaOOH through the proposed liquid−liquid dealloying strategy. Figure S4(b) in SI displays the Raman spectrum of the GaOOH−AgSn, where all six Raman scattering peaks can be assigned to the GaOOH [25]. The Raman results provide corroborating evidence of the formation of GaOOH, which is consistent with the XRD results.

To analyze the chemical states of the surface elements of the as-obtained sample, the XPS test was performed on GaOOH−AgSn (Figs. S4(c−e) in SI). The survey spectrum (Fig. S4(c) in SI) clearly reveals the presence of Ga and O elements. In addition, the weak peak of Na which comes from the NaOH residue is also observed, suggesting that element Na is not completely removed during the centrifugal cleaning process. The XPS spectrum of Ga 3d (Fig. S4(d) in SI) contains two peaks at 20.2 and 20.9 eV, corresponding to Ga $3d_{5/2}$ and Ga $3d_{3/2}$, respectively, indicating the oxidation state of Ga^{3+} [26]. As presented in Fig. S4(e) in SI, the O 1s spectrum is resolved into two peaks namely at 531.0 and 531.6 eV, respectively. The peak at 531.0 eV (OM) could be attributed to the lattice oxygen species (Ga^{3+}−O), whereas the peak at 531.6 eV is assigned to OH, which comes from the surface OH^- species [27]. The XPS results further demonstrate that the dealloyed product is GaOOH.

The morphology and structure of the prepared GaOOH−AgSn sample were characterized. A high-

magnification SEM image of the GaOOH−AgSn can be seen in Fig. 3(a), which displays that the well-parallel 1D nanostructure consists of nanowire bundles with an average width of 20−30 nm. TEM image (Fig. 3(b)) further reveals the clear outline of the ultra-fine GaOOH nanowire inside the bundles. The disclosed 1D nanowire morphology can be attributed to the fast crystal growth along the *c*-axis, which is common for GaOOH grown in aqueous solution [28]. High-resolution TEM (HRTEM) image of the sample (Fig. 3(c)) displays the clear lattice fringe with the *d*-spacing of 0.254 and 0.265 nm, corresponding to the GaOOH (021) and (130) crystal planes, respectively. The diffraction spots in the selected area electron diffraction (SAED) pattern (Fig. S5 in SI) present the (021), (131) and (110) planes of GaOOH and the corresponding $[1\bar{1}2]$ axis, confirming the single-crystalline nature of the sample.

In previous reports [28,29], taking GaOOH as the precursor, Ga_2O_3 species have been successfully synthesized by the thermal decomposition method. Significantly, the experimental temperature directly determines the phase composition of the final products due to different thermal stabilization natures of various Ga_2O_3 phases (α-Ga_2O_3 and β-Ga_2O_3, etc.). In this work, Ga_2O_3 species with different phase compositions were obtained in a calcination process under controlled temperatures.

The SEM image of the Ga_2O_3-450 product is displayed in Fig. 3(d). Clearly, the morphology of the sample consists of regular 1D nanowires. The

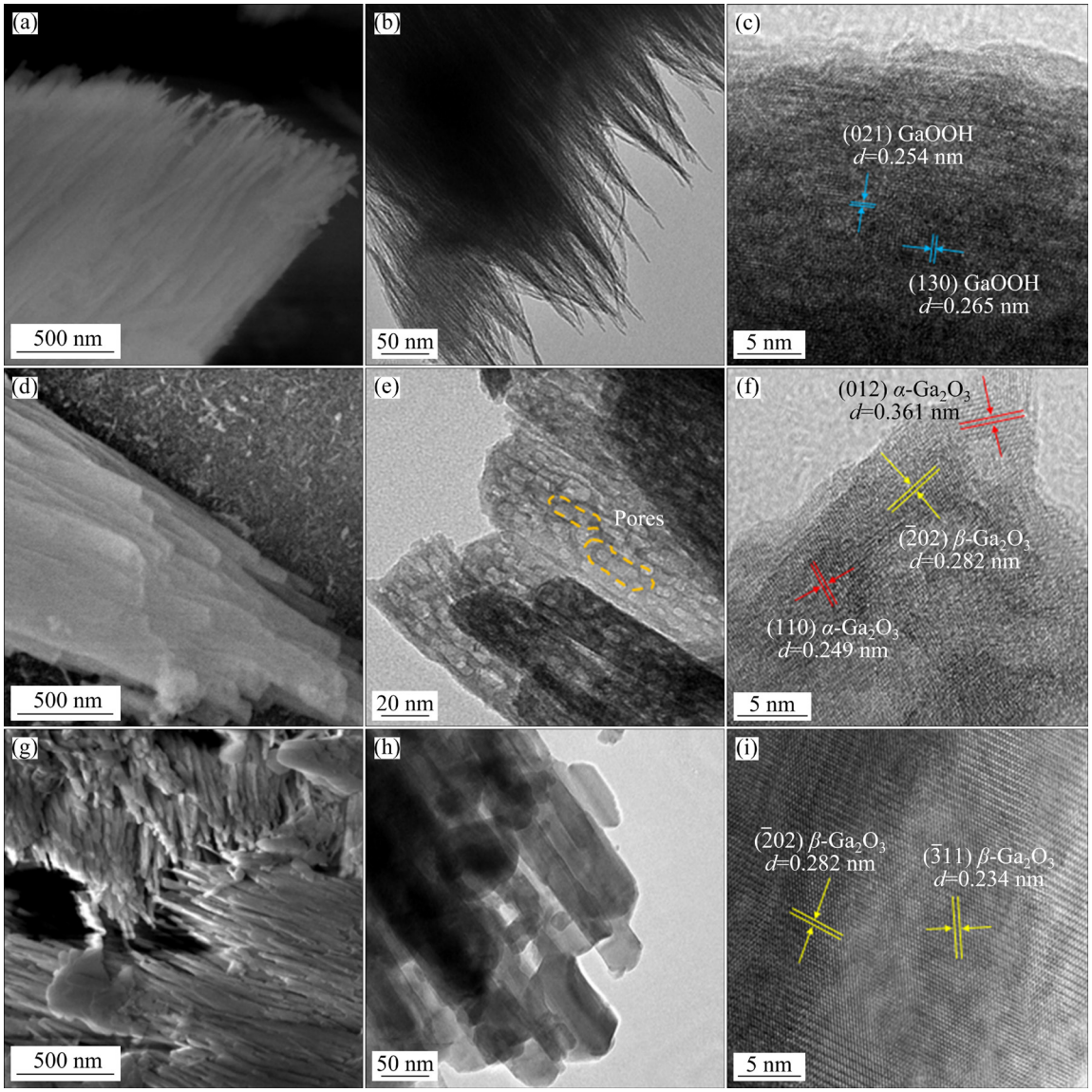

Fig. 3 SEM (a) and TEM (b, c) images of GaOOH−AgSn; SEM (d) and TEM (e, f) images of Ga_2O_3-450; SEM (g) and TEM (h, i) images of Ga_2O_3-900

observed morphology indicates that the structure of the GaOOH is well preserved during the calcination treatment process. Figure S6 in SI displays the EDS spectrum of the Ga_2O_3-450, in which the principal presence of elements Ga and O suggests the formation of Ga−O oxide. Furthermore, the structure of the Ga_2O_3−Ag and Ga_2O_3−Sn was characterized (Fig. S7 in SI). Similarly, the 1D nanowire structure also forms in the above two reference Ga_2O_3 samples. However, compared with the Ga_2O_3-450, the two reference Ga_2O_3 display irregular nanowire structures containing partially aggregation nanoparticles. The results of the morphological characterization reveal that the initial dealloying precursor's composition has a direct influence on the structure of the final products. Adjusting the component of the liquid metal precursor is a workable technique for controlling the structure of the dealloyed products.

The TEM image further reveals the morphology and structure of the Ga_2O_3-450. In correspondence with the SEM result, a typical 1D structure consisting of parallel nanowires with diameters of 25−40 nm is disclosed and shown in Fig. 3(e). Clearly, in contrast to the pristine GaOOH nanowires (Fig. 3(b)), an obvious structure coarsening occurs in the calcination process. In addition, uniform pores are created on the formed Ga_2O_3 nanowires (Fig. 3(e)). These pores are the result of the removal of hydroxyl groups in the GaOOH precursor during the calcination. Thus, to generate Ga_2O_3 with the regular structure for advanced applications, it is important to first develop a GaOOH precursor with a well-organized structure, and without structural collapse under extreme conditions of high-temperature treatment. Figure 3(f) displays a clear observation of the lattice fringes with fringe spacings of 0.249 and 0.361 nm, which correspond to the (110) and (012) crystal planes of α-Ga_2O_3, respectively. Besides, the lattice fringe with a d-spacing of 0.282 nm in accord with the $(\bar{2}02)$ crystal plane of the β-Ga_2O_3 is also observed (Fig. 3(f)). The SAED pattern (Fig. S8 in SI) of the Ga_2O_3-450 consists of concentric rings which are attributed to (104), (110) and (214) crystal planes of α-Ga_2O_3, indicating the polycrystalline nature of the sample. These results suggested that the dealloyed GaOOH is converted to α-Ga_2O_3 by the calcining process at 450 °C, and traces of β-Ga_2O_3 also form in this situation. Figure S9 in SI reveals the STEM image and the corresponding elemental mapping of the Ga_2O_3-450 sample. Obviously, both Ga and O elements are distributed uniformly, further demonstrating the formation of Ga−O oxide.

Additionally, to further understand the phase transition behavior of the dealloyed GaOOH in the calcination experiment, the structure of the Ga_2O_3-900 sample was also characterized. As revealed in Fig. 3(g), the SEM image of the Ga_2O_3-900 shows a disorderly nanowire structure with some particles agglomerating and embedding on the surface. TEM image further provides a clear observation of the structure of the sample. As shown in Fig. 3(h), the irregular nanowires and agglomerated particles can be observed. Moreover, there are no traces of pores in the TEM image, that is because the pores, pre-formed at the relatively low temperature, are reclosed during the high temperature. Figure 3(i) shows the HRTEM image of the calcined Ga_2O_3-900. The lattice fringes of 0.234 and 0.282 nm are identified as the $(\bar{3}11)$ and $(\bar{2}02)$ facets of β-Ga_2O_3, respectively. The SAED pattern (Fig. S10 in SI) of Ga_2O_3-900 displays diffraction spots assigned to $(\bar{1}10)$, (111) and (201) planes of β-Ga_2O_3 and the corresponding $[11\bar{2}]$ axis, revealing the single crystal nature of Ga_2O_3-900. These observations suggest that α-Ga_2O_3 forms at a relatively low calcination temperature, and then further converts to β-Ga_2O_3 at a higher temperature.

Figure 4(a) displays the examined XRD patterns to reveal the crystal structure of the calcined products, favoring further comprehension of the phase transition process. The diffraction peaks corresponding to (012), (104), (110), (006), (113), (024), (116), (214), and (300) crystal planes of α-Ga_2O_3 phase (JCPDS No. 06-0503) are indexed in the XRD pattern of Ga_2O_3-450 [30]. Besides, two weak peaks related to β-Ga_2O_3 phase (JCPDS No. 41-1103) can also be observed [31,32]. The characterized XRD results reveal that the Ga_2O_3-450 principally consisted of α-Ga_2O_3 phase, with traces of β-Ga_2O_3 in the sample. When the calcination temperature reaches 700 °C, the XRD pattern of the Ga_2O_3-700 sample displays a decreased intensity of characteristic peaks of α-Ga_2O_3, whereas that of β-Ga_2O_3 increases obviously. This indicates that the proportion of β-Ga_2O_3 rises under the thermal treatment at a

higher temperature. Moreover, sharp Bragg peaks with clear crystal face of β-Ga_2O_3 are well observed in the XRD pattern of Ga_2O_3-900, and the characteristic peaks of α-Ga_2O_3 almost disappear, suggesting that the calcination product at 900 °C is mainly composed of β-Ga_2O_3.

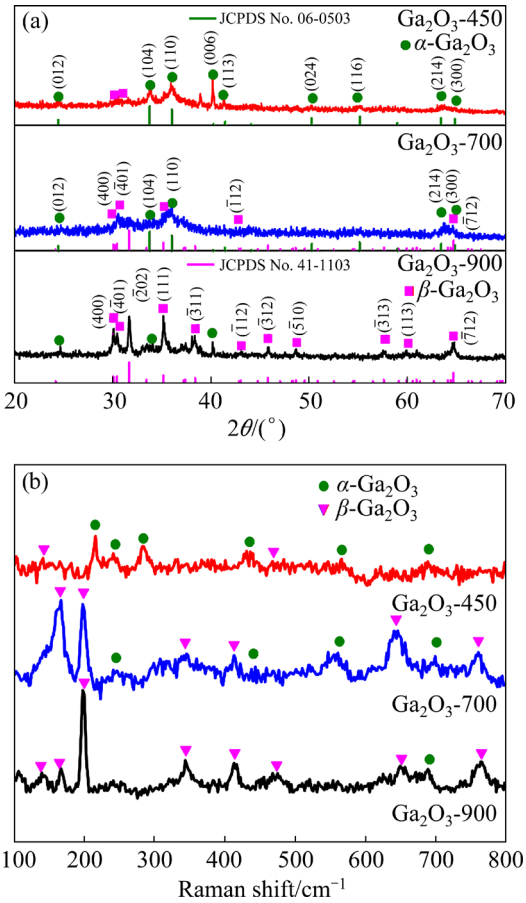

Fig. 4 XRD patterns (a) and Raman spectra (b) of Ga_2O_3-450, Ga_2O_3-700, and Ga_2O_3-900

These results allow for the reasonable hypothesis that, when the calcination temperature is raised, the dealloyed GaOOH initially transforms to α-Ga_2O_3 and then to β-Ga_2O_3. This is consistent with the phase transformation behaviors among various polymorphs of Ga_2O_3 in previous reports, since the monoclinic β-Ga_2O_3 phase is in the most thermodynamically stable form [25]. During the calcination process, the 1D structure is retained and modified gradually, which is in accord with the observed SEM and TEM results. When GaOOH decomposes to α-Ga_2O_3, the 1D skeleton remains with a smooth surface and cavities formed inside the nanowires. With the increase in calcination temperature, α-Ga_2O_3 on the surface transforms to β-Ga_2O_3 while maintaining an inner bulk region of α-Ga_2O_3. At a calcination temperature of 900 °C, α-Ga_2O_3 could be almost completely converted to β-Ga_2O_3 over time. In the second phase transition step, the 1D structure is preserved roughly, while the inside pores are fused and reassembled. Raman spectra (Fig. 4(b)) of the samples also demonstrate the phase transformation behavior during the calcination treatment. Along with the increase of the calcination temperature, the characteristic peaks corresponding to α-Ga_2O_3 gradually disappear, whereas the peaks assigned to β-Ga_2O_3 gradually dominate the Raman spectrum [33]. The verified Raman results suggest that the α-Ga_2O_3 prepared by calcining GaOOH at 450 °C, underwent a conversion from α-phase to β-phase upon increasing the calcination temperature from 450 to 900 °C, and Ga_2O_3 species with different phase composition ratios could be obtained during the phase transformation process.

In order to further uncover the structural characteristics of the product, the N_2 adsorption/desorption isotherm and corresponding pore size distribution of Ga_2O_3-450 were examined (Fig. S11(a) in SI). It can be known that the specific surface area of Ga_2O_3-450 is 97.0 m^2/g, this value benefits from the plenty of pores in the skeleton of the well-arranged nanowires. The sample presents type III isotherms with a typical H3-type loop, which demonstrates the existence of mesopores [34,35]. The observed pore size distribution (Fig. S11(b) in SI) of the sample indicates that the pores of the Ga_2O_3-450 sample mainly distribute in the range of 2−10 nm. The abundant mesopores in the sample can not only accelerate the ion transport, but also effectively alleviate the effect of volume expansion/shrinkage of the electrode materials during cycling.

XPS tests were performed to reveal the chemical state of the elements in the samples (Ga_2O_3-450, Ga_2O_3-700, and Ga_2O_3-900). The XPS full survey spectra provide evidence of the existence of elements Ga and O in the material (Fig. 5(a)). Clearly, the weak peak assigned to Na is marked in the spectra, indicating that element Na remains on the surface of the samples. High-resolution spectra of Ga 3d in Fig. 5(b) display signals of Ga spin-orbit levels. A strong peak at 20.6 eV can be assigned to the Ga—O band in Ga_2O_3 [18,36]. The XPS spectra of O 1s (Fig. 5(c)) are properly divided into two peaks. The peak at

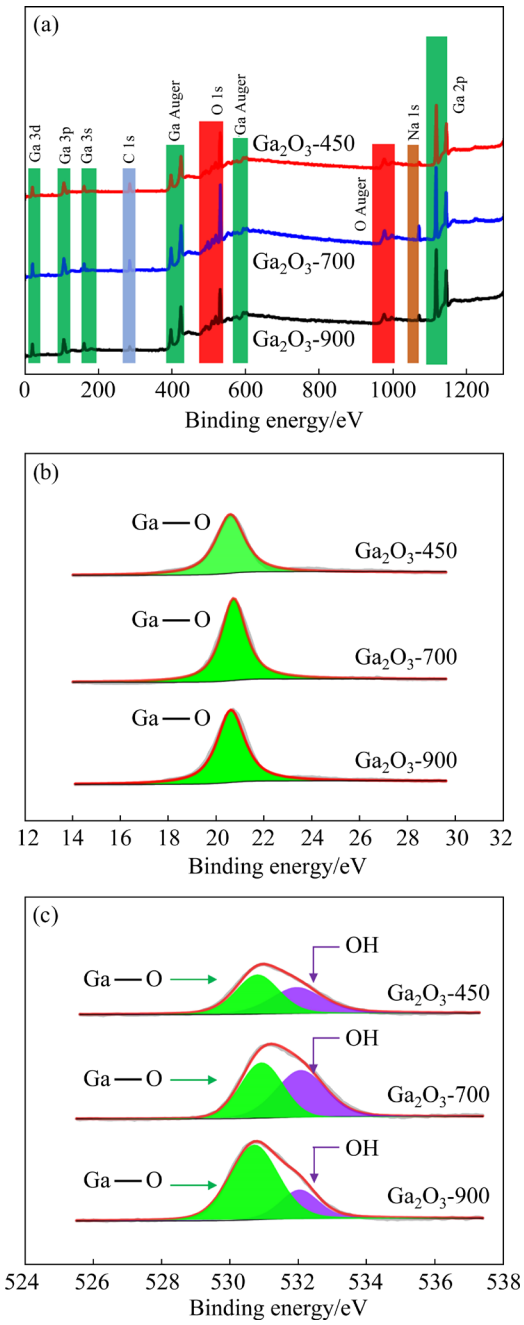

Fig. 5 XPS survey spectra of Ga_2O_3-450, Ga_2O_3-700 and Ga_2O_3-900 (a); High-resolution spectra of Ga 3d (b) and O 1s (c)

530.8 eV corresponds to lattice O^{2-} in the Ga—O band, while the peak at 532.0 eV could be related to the contributions from OH^-, which results from the residual NaOH corrodent [37].

3.2 Electrochemical performance

To reveal the electrochemical reaction mechanism, the cyclic voltammetry (CV) test was performed in a potential range of 0.01−3 V (vs Li/Li^+) with a sweep rate of 0.1 mV/s. Figure 6(a) displays the CV curves of the 1st, 2nd, and 5th scans of the CV curves of the Ga_2O_3-450 electrode. In the initial scan, the cathode peak at 0.73 V can be assigned to the conversion reaction ($Ga_2O_3 + 6Li^+ + 6e = 2Ga + 3Li_2O$), as well as the formation of a solid electrolyte interphase (SEI) layer [38]. Furthermore, the stronger cathodic peak at 0.38 V corresponds to the reversible alloying reaction ($Ga + 2Li^+ + 2e \rightarrow Li_2Ga$) [39]. In the subsequent cycles, the cathodic peaks shift to a high potential region, which can be ascribed to the activation of the electrode [40,41]. The anode peaks at 0.47 and 0.94 V are attributed to the delithiation reaction to generate Ga ($Li_2Ga = Ga + 2Li^+ + 2e$) and the partial oxidation of Ga, respectively [42]. During the lithiation/delithiation process, the generated Ga could provide the self-healing property to the electrode, to avoid the structural collapse of the electrode. The well-overlapped CV curves demonstrate the favorable reversibility of Li^+ storage.

Figure 6(b) shows the charge and discharge profiles of the Ga_2O_3-450 electrode for the 1st, 2nd, 10th, 50th, and 100th cycles in the potential range of 0.01−3.0 V at a current density of 200 mA/g. There are two potential platforms at 0.6−0.9 and 0.2−0.5 V in the initial discharge step. Meanwhile, two potential plateaus at 0.9−1.1 and 0.3−0.5 V are found in the first charge step. The observed potential ranges are basically in agreement with those in the CV curves. The Ga_2O_3-450 electrode delivers discharge and charge capacities of 1438.4 and 1063.5 mA·h/g, respectively, with a loss rate of 26.1%. The capacity fading is related to the unavoidable formation of SEI and the partial irreversible conversion reaction [18]. With increasing the cycling number, the curves gradually shift to the left, suggesting that the capacity decreases during cycling. However, the curves of the 50th and 100th are very close, which indicates the stable cycling performance in the later stage.

The cycling performance of Ga_2O_3-450, Ga_2O_3-700, and Ga_2O_3-900 electrodes in the potential range of 0.01−3 V at 200 mA/g over 100 cycles is displayed in Fig. 6(c). The Ga_2O_3-450 electrode exhibits an initial discharge capacity of 1438.4 mA·h/g with a coulombic efficiency of 73.9%, and maintains a reversible capacity of 867.1 mA·h/g after 100 cycles, showing excellent

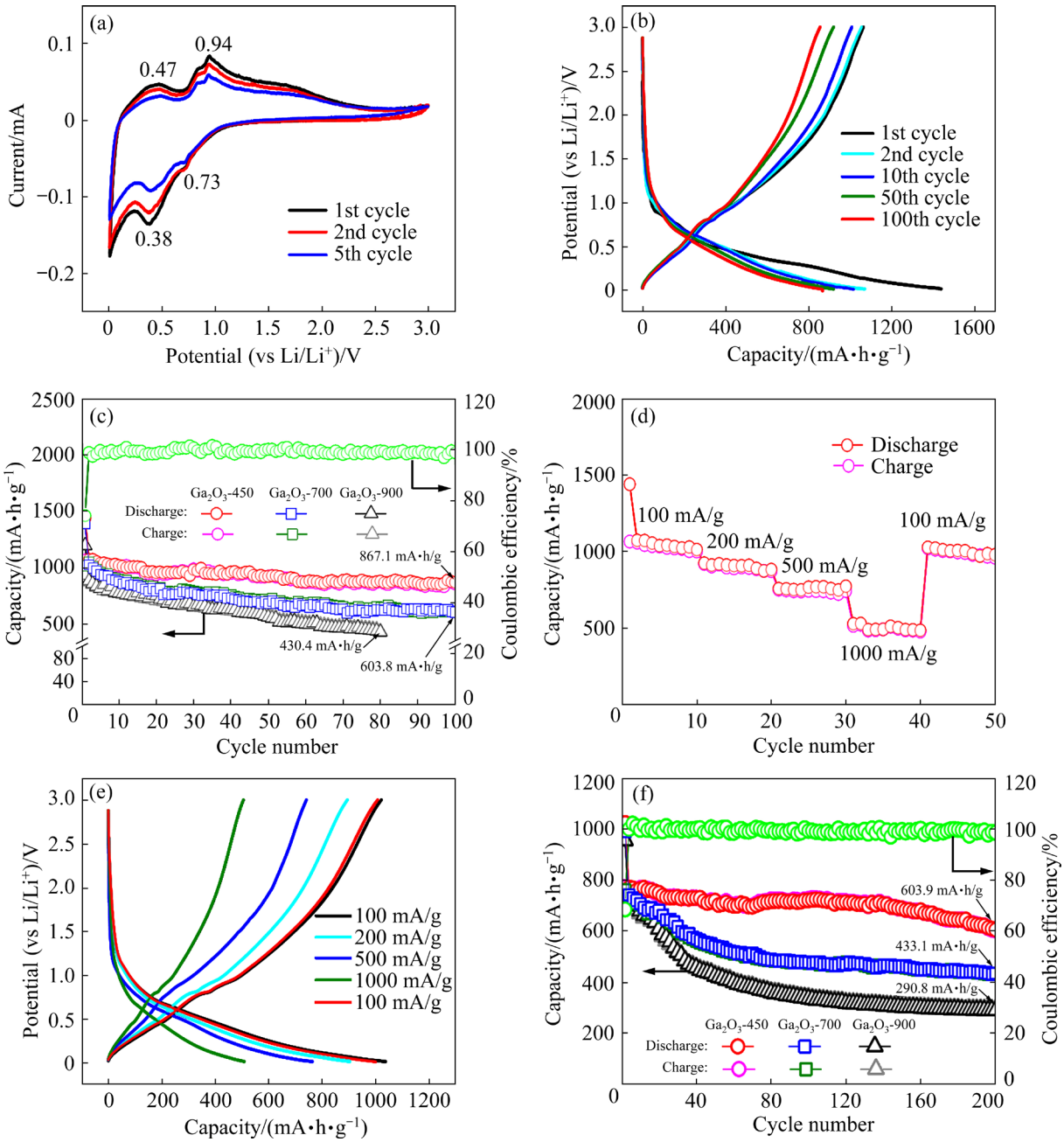

Fig. 6 (a) CV curves of Ga_2O_3-450 electrode at 0.1 mV/s; (b) Charge and discharge potential profiles of Ga_2O_3-450 electrode at 200 mA/g; (c) Cycling performance of Ga_2O_3-450, Ga_2O_3-700, and Ga_2O_3-900 at 200 mA/g; (d) Rate performance of Ga_2O_3-450 electrode at different current densities; (e) Galvanostatic charge and discharge potential profiles of Ga_2O_3-450 electrode at various current densities after 50 cycles; (f) Long-term cycling performance of Ga_2O_3-450, Ga_2O_3-700, and Ga_2O_3-900 electrodes at 1000 mA/g

cycling stability. The impressive electrochemical performance can be attributed to the porous nanowire structure. During the cycling process, the interspace inside the well-arranged nanowires and the uniformly distributed nanopores can shorten the pathway of Li ion diffusion and provide enough space to moderate the effect of volume variation of the electrode. The Ga_2O_3-700 electrode shows a stable cycling performance after 70 cycles and maintains a reversible capacity of 603.8 mA·h/g after 100 cycles. By contrast, the Ga_2O_3-900 electrode exhibits a drastic capacity decay from 1193.6 mA·h/g in the initial cycle to 434.4 mA·h/g after 80 cycles, with a capacity loss of around 0.08% per cycle. In addition to the microstructure, the active components of electrode materials are

another decisive factor for the electrochemical performance. Here, the as-displayed electrochemical performance suggests that α-Ga_2O_3 has a better Li storage capability than β-Ga_2O_3.

The rate performance of the Ga_2O_3-450 electrode was measured at current densities ranging from 100−1000 mA/g. As presented in Fig. 6(d), the Ga_2O_3-450 electrode displays an outstanding rate capability. At the current densities of 100, 200, 500, and 1000 mA/g, the Ga_2O_3-450 electrode delivers reversible capacities of 1010.2, 879.8, 770.4, and 482.2 mA·h/g, respectively. Furthermore, when the current density restores to 100 mA/g, the capacity of the Ga_2O_3-450 electrode recovers to 975.7 mA·h/g. Figure 6(e) shows the charge and discharge profiles of the Ga_2O_3-450 electrode at various current densities. Obviously, upon increasing the current densities, the potential plateau gradually shortens, indicating increased electrode polarization and reduced charge and discharge capacities. When the current density converts to 100 mA/g, the curve is nearly coincidental with the initial stage, demonstrating the excellent reversibility of the Ga_2O_3-450 electrode.

The cycling performance of Ga_2O_3-450, Ga_2O_3-700, and Ga_2O_3-900 electrodes at a high current density of 1000 mA/g for 200 cycles is displayed in Fig. 6(f). Impressively, the Ga_2O_3-450 electrode presents an outstanding long-term cycling performance, exhibiting a specific capacity of 603.9 mA·h/g with a coulombic efficiency around 98.4% after 200 cycles. According to the measured cycling results, the reversible capacity of the Ga_2O_3-450 electrode decays slowly in the first 70 cycles, and then the capacity gradually increases until 110 cycles. This capacity-increasing behavior is known among some conversion reaction-based anodes, which originates from a deactivation procedure (initial fading) when the thick SEI layers form, followed by a reactivation step that corresponds to the formation of a thinner SEI [41,43]. Following the capacity reactivation stage, the capacity remains stable for tens of cycles, and then, an obvious capacity fading phenomenon can be observed in the later stage of cycling. This capacity fading behavior may be related to the thermodynamically unstable nature of α-Ga_2O_3 phase. The displayed electrochemical performance of the Ga_2O_3-450 electrode is better than that of most of the reported Ga_2O_3-based anode materials, as shown in Table 1 [14−20,33,44]. In comparison, the Ga_2O_3-700 and Ga_2O_3-900 electrodes suffer extreme capacity deterioration, exhibiting discharge capacities of 433.1 and 290.8 mA·h/g at 1000 mA/g after 200 cycles, respectively.

Table 1 Comparison of electrochemical performance of Ga_2O_3-based anodes

Anode material	Current density/ ($mA\cdot g^{-1}$)	Cycle number	Reversible capacity/ ($mA\cdot h\cdot g^{-1}$)	Source
Ga_2O_3-rGO	50	40	770	[20]
α-Ga_2O_3@C@G	100	50	458	[33]
Ga_2O_3@rGO	100	100	428.7	[16]
Ga_2O_3/N doped C nanopapers	200	200	477	[15]
β-Ga_2O_3@G/C	500	150	379.9	[14]
γ-Ga_2O_3@C	500	200	353	[17]
γ-Ga_2O_3@C nanosheets	500	200	598	[44]
Hollow Ga_2O_3@N-CQDs	500	500	700.5	[18]
Ga_2O_3 NPs@CF	500	500	611	[19]
Porous α-Ga_2O_3 nanowires	200	100	867.1	This work
	1000	200	603.9	

The galvanostatic intermittent titration technique (GITT) tests were performed on the Ga_2O_3-based anodes (Fig. S12(a) in SI) to analyze the kinetics of lithium diffusion during lithiation/ delithiation reactions (the electrodes relaxed for 2 h after applying a pulse current density of 200 mA/g for 0.5 h). It can be found that the three anodes display similar GITT curves in shape; however, they differ in the charge and discharge duration owing to the varied reaction dynamics and reversible capacity. Based on Fick's second law, the diffusion coefficient of Li ions (D_{Li^+}) can be estimated by the following equation:

$$D_{Li^+}=\frac{4}{\pi\tau}\left(\frac{mV}{MS}\right)^2\left(\frac{\Delta E_s}{\Delta E_\tau}\right)^2$$

where τ is the constant current duration of charge and discharge pulse; m and M refer to the mass loading and molar mass of active materials, respectively; V is the molar volume and S is the

effective surface area of electrodes; ΔE_s and ΔE_τ stand for the voltage change caused by the pulse and the voltage variation induced by the constant current charge and discharge, respectively. It can be observed that the Ga_2O_3-450 electrode has a higher Li ion diffusion coefficient than the Ga_2O_3-700 and Ga_2O_3-900 electrodes during the charge and discharge process (Fig. S12(b) in SI), demonstrating the enhanced ion transport kinetics.

EIS tests were performed to reveal the charge-transfer kinetics of the Ga_2O_3-450 electrode. Figure S13 in SI displays the EIS spectra and the corresponding equivalent circuit model (inset) of the sample. Nyquist plots contain a slope line at low frequency and a semicircle at high frequency, corresponding to the Warburg resistance of Li^+ diffusion (Z_W) and charge-transfer resistance (R_{ct}), respectively. The constant phase element (CPE) refers to the elements at the interface between the electrode and electrolyte. It can be seen that the impedance of the Ga_2O_3-450 electrode decreases obviously after 100 cycles, which is attributed to the surface activation of the electrode. However, it is challenging to discern information between R_{ct} and R_{SEI} because the SEI layer's growth is restricted to form a thinner SEI layer during cycling. These findings demonstrate that the constructed regular porous 1D nanowire structure is advantageous for gaining access to a quick charge/ion-transfer rate and for further improving electrochemical performance.

3.3 Lithium storage mechanism

To further reveal the lithium storage mechanism, ex-situ Raman measurements were carried out on the Ga_2O_3-450 electrode under different states of charge and discharge. As shown in Fig. 7(a), the electrode reflects obvious α-Ga_2O_3 peaks at the open circuit potential around 2.2 V. When discharging to 0.73 V and further to 0.37 V, the peaks assigned to α-Ga_2O_3 phase significantly weaken, which could be ascribed to the conversion process from Ga_2O_3 to Ga. Moreover, the peaks corresponding to β-Ga_2O_3 phase appear in this case [33]. This result suggests that in the first lithiation reaction step, as α-Ga_2O_3 on the superficial space gradually converted to Ga, partial α-Ga_2O_3 phases which remain inside the bulk region of Ga_2O_3-450, spontaneously transformed to β-Ga_2O_3 phases. The observed phase transition behavior may be actuated by the stress that comes from the volume change of the electrode materials [45,46]. Along with the lithiation process continuing (Ga_2O_3 converts to Ga and the further lithiation process from Ga to Li_2Ga), the peaks related to Ga_2O_3 phases gradually decrease and almost disappear when discharging to 0.01 V. In the charge stage, the peaks attributed to α-Ga_2O_3 phase recover upon charging to 0.94 V, whereas the weak peaks corresponding to β-Ga_2O_3 are also observed in this situation, demonstrating that Ga that is generated during the delithiaition step further oxidizes to Ga_2O_3 phases [42]. When charging to

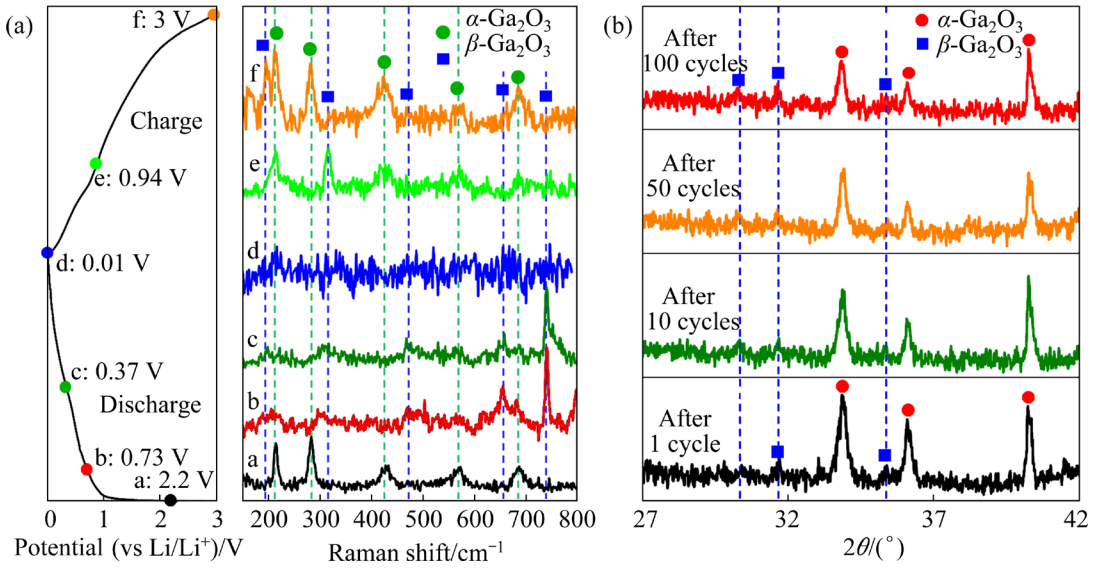

Fig. 7 (a) Ex-situ Raman spectra of Ga_2O_3-450 electrode under various discharge and charge states; (b) Ex-situ XRD patterns of Ga_2O_3-450 electrode after different cycles

3.0 V, the peaks that belong to α-Ga_2O_3 and β-Ga_2O_3 are further enhanced, suggesting that the oxidation reaction continuously proceeds. In addition, ex-situ Raman results demonstrate that during an electrochemical lithiation/delithiation cycle, the partial α-Ga_2O_3 phase of the Ga_2O_3-450 will transform to more thermodynamically stable β-Ga_2O_3, which may be one of the reasons why battery capacity continues to slowly decline.

The ex-situ XRD patterns during cycling provided additional confirmation of the phase transition behavior (Fig. 7(b)). With the increase in the cycle number, the intensity of diffraction peaks of α-Ga_2O_3 gradually decreases while the intensity of diffraction signals of β-Ga_2O_3 phase is gradually enhanced. As a result, the Ga_2O_3-450 electrode exhibits the clear coexistence of α-Ga_2O_3 and β-Ga_2O_3 phases after 100 cycles.

It can be observed from ex-situ TEM results (Figs. 8(a, d)) that the Ga_2O_3-450 maintains a well-defined nanowire bundle structure without structural collapse after 10 cycles and even up to 100 cycles at 200 mA/g, proving that the prepared porous nanowire structure can effectively alleviate the huge volume variation during cycling and be advantageous for achieving excellent cycling stability. Due to the decoration of conductive agent (Super P) and binder (CMC) during the preparation of working electrodes, it is difficult to characterize the porosity of cycled Ga_2O_3-450 electrodes clearly. According to the existing TEM images, although the pore numbers in nanowires gradually decrease after many cycles, it can be observed that there is still a certain volume of pores in the nanowires. These residual pores undoubtedly play an important role in the electrochemical process. The HRTEM image of Ga_2O_3-450 anode after 10 cycles displays lattice fringes corresponding to (110) and (104) crystal planes of α-Ga_2O_3 phase and (111) plane of β-Ga_2O_3 phase (Fig. 8(b)). The SAED pattern in Fig. 8(c) exhibits the typical polycrystalline diffraction rings and shows the coexistence of α-Ga_2O_3 and β-Ga_2O_3 phases, which further demonstrates the phase transition behavior from α-Ga_2O_3 to β-Ga_2O_3 during cycling. As the lithiation/delithiation cycle progresses, more crystal planes belonging to β-Ga_2O_3 phase are exposed on α-Ga_2O_3 substrate (Figs. 8(e, f)).

Based on the aforementioned findings, it can be suggested that the Ga_2O_3-450 anode experiences a spontaneous phase change from α-Ga_2O_3 to β-Ga_2O_3 during cycling, and maintains a bulk region

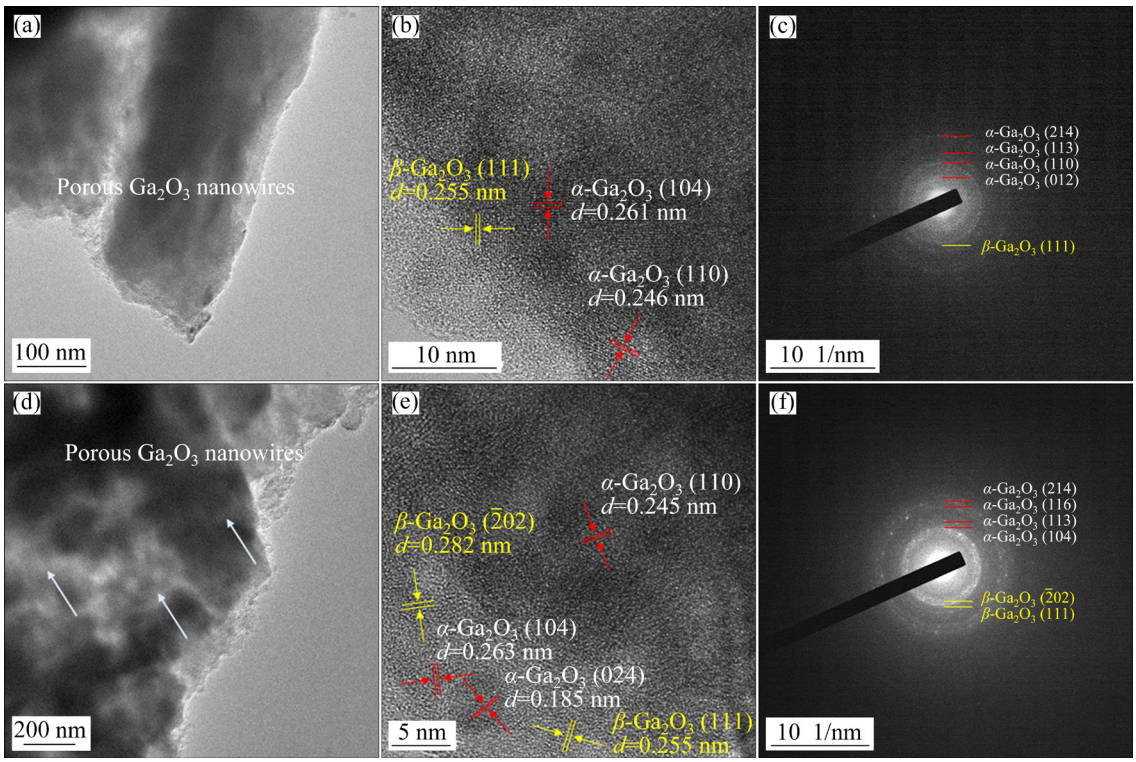

Fig. 8 TEM image (a), HRTEM image (b), and SAED pattern (c) of Ga_2O_3-450 electrode after 10 cycles at 200 mA/g; TEM image (d), HRTEM image (e), and SAED pattern (f) of Ga_2O_3-450 electrode after 100 cycles at 200 mA/g

of pristine α-Ga_2O_3 phase with a part of β-Ga_2O_3 after cycling. Moreover, these findings also suggest that the capacity fading phenomenon in the later stage of cycling of the Ga_2O_3-450 electrode is related to the phase transformation (from α-Ga_2O_3 to β-Ga_2O_3) and structural changes.

The density functional theoretical (DFT) based first principle calculations were carried out to make a better understanding of the electrochemical behavior of Ga_2O_3 electrodes with different phase compositions. The crystal structures of α-Ga_2O_3 and β-Ga_2O_3 were constructed and displayed in Figs. S14(a, b) in SI, respectively. α-Ga_2O_3 owns the *R-3C* symmetry, whereas β-Ga_2O_3 has the *C*2/*m* symmetry. Figures S15 and S16 in SI show the optimized Li adsorption configurations, whereas the calculated Li adsorption energy on the surface of α-Ga_2O_3 and β-Ga_2O_3 is displayed in Fig. 9(a). The adsorption energies of the two adsorption sites (Site I and Site II) of α-Ga_2O_3 are evaluated as −2.3 and −2.8 eV, respectively, which are much lower than that of the β-Ga_2O_3 (−0.9 and −1.0 eV), suggesting a higher Li adsorption capability of α-Ga_2O_3 than β-Ga_2O_3.

The charge density difference of Li for α-Ga_2O_3 and β-Ga_2O_3 at Site II is further elucidated and shown in Figs. 9(b, c) and Fig. S17 in SI, in which the charge depletion (cyan electron clouds) and the charge accumulation (yellow electron clouds) constitute the charge redistribution behavior [47]. The results suggest that there exists a strong electronic coupling between Li and the surface of α-Ga_2O_3. Furthermore, the larger electron cloud density of the α-Ga_2O_3 system compared to the β-Ga_2O_3 system suggests that the α-Ga_2O_3 system possesses a stronger capacity for Li adsorption, which is consistent with the calculated Li adsorption energy.

According to the density of state (DOS), both α-Ga_2O_3 (Fig. 9(d)) and β-Ga_2O_3 (Fig. 9(e)) have the typical semiconductor property with poor electrical conductivity, generally giving rise to sluggish electrochemical reaction kinetics. However, the revealed bandgap of ~1.47 eV for α-Ga_2O_3 is smaller than that of β-Ga_2O_3 (~1.62 eV), suggesting the faster surface electronic transport kinetics during lithiation/delithiation reactions [48].

The DFT calculation results suggest the stronger Li adsorption ability and the improved electrochemical reaction kinetics of α-Ga_2O_3 compared

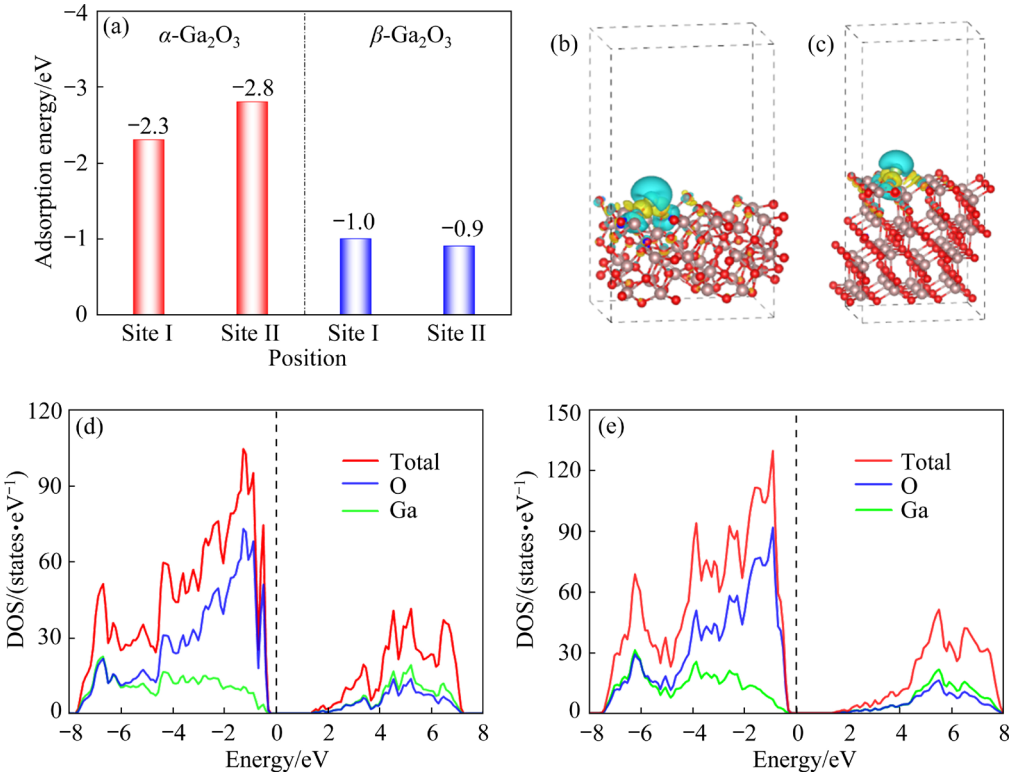

Fig. 9 (a) Calculated Li adsorption energy on surface of α-Ga_2O_3 and β-Ga_2O_3; (b, c) Charge density differences of Li adsorption on surface of α-Ga_2O_3 and β-Ga_2O_3, respectively; (d, e) Density of states (DOS) curves of α-Ga_2O_3 and β-Ga_2O_3, respectively

to β-Ga_2O_3, thus resulting in excellent electrochemical performance. Drawing on the aforementioned findings, a plausible hypothesis is put forth that the phase transition from α-Ga_2O_3 to β-Ga_2O_3 occurs during cycling, leading to the capacity fading behavior of the Ga_2O_3-450 anode towards the later stage of the cycle. The disclosed electrochemical reaction mechanism of Ga_2O_3 anodes in this work provides a significant reference to the rational design of Ga_2O_3-based anodes.

3.4 Full cells performance

To evaluate the practical possibility of the as-prepared porous Ga_2O_3 nanowires anodes, full cells coupled by porous Ga_2O_3 nanowires anodes and a commercialized $LiFePO_4$ cathode were assembled (Fig. S18 in SI). All the anodes were pre-lithiated to 0.05 V by electrochemical discharging before full cells assembling. Figure S19 in SI and Fig. 10(a) disclose the typical charge and discharge curves of the Ga_2O_3-450 anode, the $LiFePO_4$ cathode, and the constructed Ga_2O_3-450//$LiFePO_4$ full cell, respectively. The Ga_2O_3-450//$LiFePO_4$ full cell delivers initial charge and discharge capacities of 163.4 and 155.9 mA·h/g, respectively. The initial capacity loss could be caused by the decomposition of the electrolyte or the development of a cathode electrolyte interface (CEI) [49]. At the current density of 0.5C (1C=170 mA/g), the built Ga_2O_3-450//$LiFePO_4$ full cell experiences a reversible capacity of 125.2 mA·h/g after 100 cycles, showing a significantly enhanced capacity retention compared to full cells adopted with Ga_2O_3-700 anode (50.8 mA·h/g) and Ga_2O_3-900 anode (36.3 mA·h/g) (Fig. 10(b)). The exceptional cycle stability of Ga_2O_3-450//$LiFePO_4$ full cell can be traced to the advanced porous nanowire structure and stable SEI film of Ga_2O_3-450 anode.

The rate performance of the assembled full cells was further examined. As displayed in Fig. 10(c), the Ga_2O_3-450//$LiFePO_4$ full cell shows superior rate performance with reversible capacities of 146.5, 138.0, 123.3, 110.3, and 97.8 mA·h/g under the conditions of 0.2C, 0.5C, 1C, 1.5C, and 2C, respectively, exhibiting a much better capacity maintaining capability as compared to the full cells

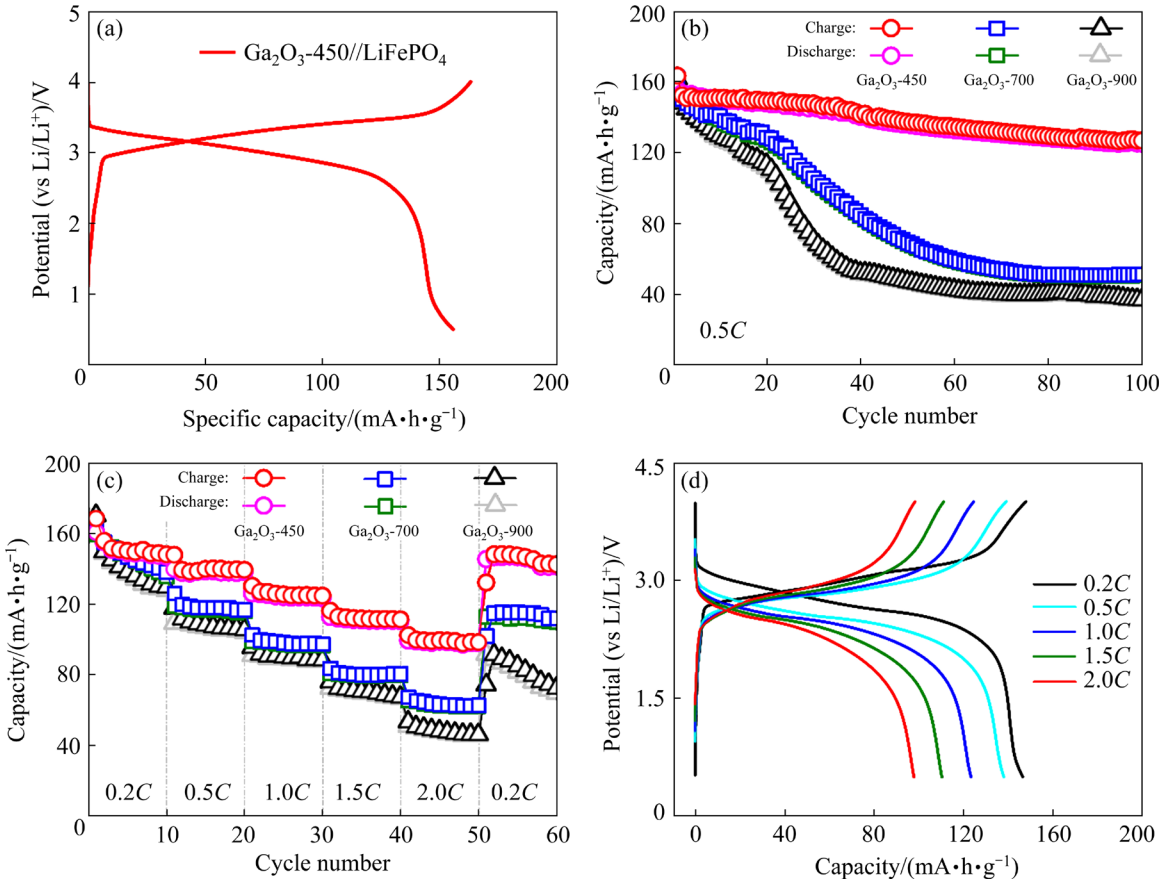

Fig. 10 (a) Typical charge and discharge profiles of Ga_2O_3-450//$LiFePO_4$ full cell; (b) Cycling performance of full cells at 0.5C; (c) Rate performance of full cells from 0.2C to 2C; (d) Charge and discharge curves of Ga_2O_3-450//$LiFePO_4$ full cell at different current densities

consisting of Ga_2O_3-700 and Ga_2O_3-900 anodes. Moreover, when restoring the current density to 0.2*C*, the reversible capacity of Ga_2O_3-450// $LiFePO_4$ full cell maintains at 141.3 mA·h/g after 10 cycles, further demonstrating a superior rate tolerance performance.

The charge and discharge curves of the Ga_2O_3-450//$LiFePO_4$ full cell at different current densities are shown in Fig. 10(d). The well-overlapping charge and discharge curves indicate that the full cell has a small polarity, which is indicative of an efficient electron/ion transport. The electrochemical behaviors of Ga_2O_3-450//$LiFePO_4$ full cells prove the potential of the as-synthesized porous Ga_2O_3-450 nanowire anode as the prospective candidate for high-performance LIBs. Furthermore, the proposed liquid−liquid dealloying strategy is highly expected to promote the extensive application of dealloying technology in the fabrication of various nano-functional materials.

4 Conclusions

(1) The porous Ga_2O_3 nanowires were prepared using a liquid−liquid dealloying method and the subsequent calcination approach. The materials can be used as an anode material for LIBs.

(2) The Ga_2O_3-450 sample revealed superior Li storage properties both in half and full battery tests. It can deliver a reversible capacity of 603.9 mA·h/g after 200 cycles at 1000 mA/g when used as an anode of a half battery. Furthermore, the built Ga_2O_3-450//$LiFePO_4$ full cell presented a reversible capacity of 125.2 mA·h/g after 100 cycles at 0.5*C*, demonstrating the promising potential of the practical application of the as-prepared Ga_2O_3-450 anode.

(3) The outstanding electrochemical performance can be related to the well-designed porous 1D nanowire structure, which is crucial for achieving quick electron and ion diffusion as well as for efficiently accommodating the volume expansion of electrode materials during lithiation/delithiation cycling.

(4) The ex-situ Raman, XRD, TEM, and DFT calculations reveal that the capacity loss behavior in the later stage of cycling is related to the phase transformation from α-Ga_2O_3 to β-Ga_2O_3 and structural changes in pore size in which the pore size reduces with the repeated charge and discharge processes and the increase in cycle number.

CRediT authorship contribution statement

Chang LUO: Conceptualization, Investigation, Formal analysis, Writing − Original draft; **Zi-gang WANG:** Methodology, Investigation, Formal analysis, Visualization; **Yi-chao WANG:** Formal analysis, Supervision, Project administration; **Shuai-ju MENG:** Investigation, Resources, Supervision; **Hui YU:** Investigation, Supervision; **Wei-min ZHAO:** Resources, Supervision; **Chun-ling QIN:** Methodology, Data curation, Resources; **Zhi-feng WANG:** Supervision, Project administration, Funding acquisition, Writing − Review & editing.

Declaration of competing interest

The authors declare that they have no known competing financial interests or personal relationships that could have appeared to influence the work reported in this paper.

Acknowledgments

The authors would like to acknowledge the financial support from the Natural Science Foundation of Hebei Province, China (No. E2023202253), and Hebei Higher Education Teaching Reform Research and Practice Project, China (No. 2021GJJG050).

Supporting Information

Supporting Information in this paper can be found at: http://tnmsc.csu.edu.cn/download/19-p3074-2024-0038-Supporting_Information.pdf.

References

[1] SUN Xia, QIN Chun-ling, ZHAO Bo-yang, JIA Shu-feng, WANG Zhi-feng, YANG Ting-zhou, LIU Xuan-cheng, PAN Li-ning, ZHENG Li-li, LUO Dan, ZHANG Yong-guang. A cation and anion dual-doping strategy in novel Li-rich Mn-based cathode materials for high-performance Li metal batteries [J]. Energy Storage Materials, 2024, 70: 103559.

[2] LIAN Meng-chen, SUN Qiang-chao, NIE Wei, LIU Yan-bo, DUAN Tong, CHENG Hong-wei, LU Xiong-gang. Na^+-doped layered $LiNi_{1/3}Co_{1/3}Mn_{1/3}O_2$ cathode derived from low nickel matte with high structural stability and fast diffusion kinetics [J]. Transactions of Nonferrous Metals Society of China, 2023, 33: 3100−3112.

[3] ZHANG An-wei, WANG Cheng-yun, FAN Wei-zhen, ZHAO Jing-wei, HUO Yan-ping, XU Xi-jun. Anhydride type film-forming electrolyte additives for high-temperature $LiNi_{0.6}Co_{0.2}Mn_{0.2}O_2$//graphite pouch cells [J]. Progress in Natural Science: Materials International, 2023, 33: 320−327.

[4] WANG Zhi-feng, YAN Ya-jing, ZHANG Yong-guang, CHEN Yan-xu, PENG Xian-yun, WANG Xin, ZHAO Wei-min, QIN Chun-ling, LIU Qian, LIU Xi-jun, CHEN

Zhong-wei. Single-atomic Co−B_2N_2 sites anchored on carbon nanotube arrays promote lithium polysulfide conversion in lithium−sulfur batteries [J]. Carbon Energy, 2023, 5: e306.

[5] LI Hui-xue, XU Xi-jun, LI Fang-kun, ZHAO Jing-wei, JI Shao-min, LIU Jun, HUO Yan-ping. Defects-abundant Ga_2O_3 nanobricks enabled multifunctional solid polymer electrolyte for superior lithium-metal batteries [J]. Chemistry, 2023, 29: e202204035.

[6] WANG Zhi-feng, WANG Hong-ying, LIU Xiao-li, CHEN Yan-xu, ZHAO Yan, ZHANG Yong-guang, HAN Qi-qi, QIN Chun-ling, BAKENOV Z, WANG Yi-chao, WANG Xin. Single Zn atoms anchored on hollow carbon nanofiber network for dendrite-free lithium metal anode of flexible Li-S full cell [J]. Rare Metals, 2023, 42(11): 3705−3717.

[7] HUANG Yu-zhu, XING Lin, PEI Shuang, ZHOU Wei, HU Yu-jie, DENG Wei-na, CHEN Wei-na, ZHU Hai, CHEN Hai. Co_9S_8/CNTs microspheres as superior-performance cathodes in aqueous ammonium-ion batteries [J]. Transactions of Nonferrous Metals Society of China, 2023, 33: 3452−3464.

[8] SHEN Hua-qing, JING Sheng-hao, LIU Si-liang, HUANG Yu-ting, HE Fang-bo, LIU Yang, ZHUANG Zhi, ZHANG Zong-liang, LIU Fang-yang. Tailoring the electronic conductivity of high-loading cathode electrodes for practical sulfide-based all-solid-state batteries [J]. Advanced Powder Materials, 2023, 2: 100136.

[9] LIANG Wen-tao, HONG Liang, YANG Hui, FAN Fei-fei, LIU Yang, LI Hong, LI Ju, HUANG Jian-yu, CHEN Long-qing, ZHU Ting, ZHANG Su-lin. Nanovoid formation and annihilation in gallium nanodroplets under lithiation−delithiation cycling [J]. Nano Letters, 2013, 13: 5212−5217.

[10] ZHU Jian-hua, WU Ying-peng, HUANG Xing-kang, HUANG Lu, CAO Meng-yang, SONG Gan-qiang, GUO Xiao-ru, SUI Xiao-yu, REN Ren, CHEN Jun-hong. Self-healing liquid metal nanoparticles encapsulated in hollow carbon fibers as a free-standing anode for lithium-ion batteries [J]. Nano Energy, 2019, 62: 883−889.

[11] JUNG J W, KIM C H, CHEONG J Y, KIM I D. Gallium nitride nanoparticles embedded in a carbon nanofiber anode for ultralong-cycle-life lithium-ion batteries [J]. ACS Applied Materials Interfaces, 2019, 11: 44263−44269.

[12] SHI Yu-jun, SONG Mei-jia, ZHANG Ying, ZHANG Chi, GAO Hui, NIU Jia-zheng, MA Wen-sheng, QIN Jing-yu, ZHANG Zhong-hua. A self-healing $CuGa_2$ anode for high-performance Li ion batteries [J]. Journal of Power Sources, 2019, 437: 226889.

[13] SUN Chang-long, TANG Xiao-fu, YIN Zheng-mao, LIU Dan, WANG Yan-jie, YANG Guan-jun, IGNASZAK A, ZHANG Jiu-jun. Self-supported GaN nanowires with cation-defects, lattice distortion, and abundant active sites for high-rate lithium-ion storage [J]. Nano Energy, 2020, 68: 104376.

[14] YANG Shu-yue, CHEN Qi-chang, NI Shi-bing, XU Zhen, ZHANG Dong-mei, LI Tao, YANG Xue-lin. Enhanced lithium ion storage in dual carbon decorated β-Ga_2O_3 rendered by improved reaction kinetics [J]. Journal of Alloys and Compounds, 2020, 828: 154484.

[15] XU Zhen, LI Dao-bo, ZHANG Dong-mei, XU Jie, LU Jun-lin, NI Shi-bing. Scalable synthesis of Ga_2O_3/N-doped C nanopapers as high-rate performance anode for Li-ion batteries [J]. ChemElectroChem, 2021, 8: 3304−3310.

[16] ZHAO Fan, DU Hui-ling, LI Zhuo, LI Qian-qian, LU Jie, CAO Na, SHI Yu-pu. Multiscale bridged and synergistic interface engineering of Ga_2O_3@rGO as an anode for lithium-ion batteries [J]. Chemical Physics Letters, 2024, 839: 141123.

[17] TANG Xun, HUANG Xin, HUANG Yong-min, GOU Yong, PASTORE J, YANG Yao, XIONG Yin, QIAN Jiang-feng, BROCK J D, LU Jun-tao, XIAO Li, ABRUÑA H D, ZHUANG Lin. High-performance Ga_2O_3 anode for lithium-ion batteries [J]. ACS Applied Materials Interfaces, 2018, 10: 5519−5526.

[18] GUO Jia-qi, GAO Fang-liang, LI Dong-yang, LUO Xing-jun, SUN Yi-ming, WANG Xing-fu, RAN Zhi-lin, WU Qi-bao, LI Shu-ti. Novel strategy of constructing hollow Ga_2O_3@N-CQDs as a self-healing anode material for lithium-ion batteries [J]. ACS Sustainable Chemistry & Engineering, 2020, 8: 13692−13700.

[19] LV Ya-min, HU Jin, FU Jia-xin, WANG Jing, WANG Kai-jun, ZHANG Wei-jun, WANG Kai-zhao. Gallium oxide particles encapsulated in carbon fiber serve as freestanding electrodes for lithium-ion batteries [J]. Ionics, 2024, 30: 2577−2583.

[20] PATIL S B, KIM I Y, GUNJAKAR J L, OH S M, EOM T, KIM H, HWANG S J. Phase tuning of nanostructured gallium oxide via hybridization with reduced graphene oxide for superior anode performance in Li-ion battery: An experimental and theoretical study [J]. ACS Applied Materials Interfaces, 2015, 7: 18679−18688.

[21] LI Man, LIU Jiang-yun, WANG Chao-yang, LIU Yang, SUN Yun-tao, QIN Chun-ling, WANG Zhi-feng, LI Yong-yan, LIU Li, LIU Shu-ming. Controllable nanoporous copper synthesized by dealloying metallic glasses: New insights into the tuning pore structure and applications [J]. Chemical Engineering Journal, 2022, 427: 130861.

[22] WANG Zhen-bin, GAO Hui, NIU Jia-zheng, ZHANG Chi, ZHANG Zhong-hua. Transforming bulk metals into metallic nanostructures: A liquid-metal-assisted top-down dealloying strategy with sustainability [J]. ACS Sustainable Chemistry Engineering, 2019, 7: 3274−3281.

[23] QIU Hua-jun, PENG Liang, LI Xiao, XU Hai-tao, WANG Yan-wei. Using corrosion to fabricate various nanoporous metal structures [J]. Corrosion Science, 2015, 92: 16−31.

[24] WANG Pei, LIU Miao, MO Fang-jie, LONG Zi-yao, FANG Fang, SUN Da-lin, ZHOU Yong-ning, SONG Yun. Exploring the sodium ion storage mechanism of gallium sulfide (Ga_2S_3): A combined experimental and theoretical approach [J]. Nanoscale, 2019, 11: 3208−3215.

[25] ZHAO Yan-yan, YANG Jing, FROST R L. Raman spectroscopy of the transition of α-gallium oxyhydroxide to β-gallium oxide nanorods [J]. Journal of Raman Spectroscopy, 2008, 39: 1327−1331.

[26] HUANG Pan-qi, LUAN Jing-fei. Preparation and characterization of an Ag_3PO_4/GaOOH composite with enhanced photocatalytic performance toward rhodamine B [J]. New Journal of Chemistry, 2020, 44: 2414−2422.

[27] LIU Yan-ping, XU Chen-xi, REN Wen-qing, HU Li-ying, FU Wen-bin, WANG Wei, YIN Hong, HE Bin-hong, HOU Zhao-hui, CHEN Liang. Self-template synthesis of peapod-like MnO@N-doped hollow carbon nanotubes as an advanced anode for lithium-ion batteries [J]. Rare Metals, 2023, 42: 929−939.

[28] DING Sha, LU Ping, ZHENG Jian-guo, YANG Xian-feng, ZHAO Fu-li, CHEN Jian, WU Hao, WU Ming-mei. Textured tubular nanoparticle structures: Precursor-templated synthesis of GaN sub-micrometer sized tubes [J]. Advanced Functional Materials, 2007, 17: 1879−1886.

[29] ZHANG Ming-xiang, ZHAO Chang-hui, GONG Hui-min, NIU Gao-qiang, WANG Fei. Porous GaN submicron rods for gas sensor with high sensitivity and excellent stability at high temperature [J]. ACS Applied Materials Interfaces, 2019, 11: 33124−33131.

[30] CHEN Peng, LI Kang-lu, LEI Ben, CHEN Lü-cun, CUI Wen, SUN Yan-juan, ZHANG Wen-dong, ZHOU Ying, DONG Fan. Crystal-structure-dependent photocatalytic redox activity and reaction pathways over Ga_2O_3 polymorphs [J]. ACS Applied Materials & Interfaces, 2021, 13: 50975−50987.

[31] LIU Jin, LU Wei, ZHONG Qian, WU Hong-zhang, LI Yun-lin, LI Li-li, WANG Zhen-ling. Effect of pH on the microstructure of beta-Ga_2O_3 and its enhanced photocatalytic activity for antibiotic degradation [J]. Journal of Colloid and Interface Science, 2018, 519: 255−262.

[32] WANG Xiang, XU Qian, LI Ming-run, SHEN Shuai, WANG Xiu-li, WANG Yao-chuan, FENG Zhao-chi, SHI Jing-ying, HAN Hong-xian, LI Can. Photocatalytic overall water splitting promoted by an α−β phase junction on Ga_2O_3 [J]. Angewandte Chemie International Edition, 2012, 51: 13089−13092.

[33] NI Shi-bing, CHEN Qi-chang, LIU Ji-lei, YANG Shu-yue, LI Tao, YANG Xue-lin, ZHAO Jin-bao. New insights into the Li-storage mechanism in α-Ga_2O_3 anode and the optimized electrode design [J]. Journal of Power Sources, 2019, 433: 126681.

[34] VARDAST N, HAGHIGHI M, ZEINALZADEH H. Catalytic properties/performance evolution during sono-hydrothermal design of nanocrystalline ceria over zinc oxide for biofuel production [J]. Chemical Engineering Journal, 2022, 430: 132764.

[35] CHEN Pei-yu, LI Ying-hui, CHENG Xiao-long, YU Hui-li, YIN Xiao-feng, JIANG Yu, ZHANG Hui, LI Shi-kuo, HUANG Fang-zhi. Tuning hierarchical structure of probiotics-derived porous carbon for potassium-ion batteries [J]. Journal of Power Sources, 2023, 574: 233164.

[36] MOON S, LEE D, PARK J, KIM J. 2D amorphous GaO_x gate dielectric for β-Ga_2O_3 field-effect transistors [J]. ACS Applied Materials Interfaces, 2023, 15: 37687−37695.

[37] YANG Yan, LIU Wei-ming, HUANG Tian-tian, QIU Meng-xia, ZHANG Rui, YANG Wan-li, HE Jun-bo, CHEN Xin, DAI Ning. Low deposition temperature amorphous ALD-Ga_2O_3 thin films and decoration with MoS_2 multilayers toward flexible solar-blind photodetectors [J]. ACS Applied Materials Interfaces, 2021, 13: 41802−41809.

[38] YANG Ming-zhi, SU Chang-long, WANG Tai-lin, CHEN Fu-zhou, SUN Ming-lei, ZHANG Lei, SHAO Yong-liang, WU Yong-zhong, HAO Xiao-peng. Graphene-oxide-assisted synthesis of Ga_2O_3 nanosheets/reduced graphene oxide nanocomposites anodes for advanced alkali-ion batteries [J]. ACS Applied Energy Materials, 2018, 1: 4708−4715.

[39] ZHANG C F, PARK S H, RONAN O, HARVEY A, ASCASO A S, LIN Z F, MCEVOY N, BOLAND C S, BERNER N C, DUESBERG G S, ROZIER P, COLEMAN J N, NICOLOSI V. Enabling flexible heterostructures for Li-ion battery anodes based on nanotube and liquid-phase exfoliated 2D gallium chalcogenide nanosheet colloidal solutions [J]. Small, 2017, 13: 1701677.

[40] NGUYEN T P, GIANG T T, KIM I T. Restructuring NiO to $LiNiO_2$: Ultrastable and reversible anodes for lithium-ion batteries [J]. Chemical Engineering Journal, 2022, 437: 135292.

[41] SUN Bao-yu, LOU Shuai-feng, ZHENG Wei, QIAN Zheng-yi, CUI Can, ZUO Peng-jian, DU Chun-yu, XIE Jing-ying, WANG Jia-jun, YIN Ge-ping. Synergistic engineering of defects and architecture in Co_3O_4@C nanosheets toward Li/Na ion batteries with enhanced pseudocapacitances [J]. Nano Energy, 2020, 78: 105366.

[42] GUO Xue-lin, DING Yu, XUE Lei-gang, ZHANG Le-yuan, ZHANG Changkun, GOODENOUGH J B, YU Gui-hua. A self-healing room-temperature liquid-metal anode for alkali-ion batteries [J]. Advanced Functional Materials, 2018, 28: 1804649.

[43] SUN Hong-tao, XIN Guo-qing, HU Tao, YU Ming-peng, SHAO Da-li, SUN Xiang, LIAN Jie. High-rate lithiation-induced reactivation of mesoporous hollow spheres for long-lived lithium-ion batteries [J]. Nature Communications, 2014, 5: 4526.

[44] JEON I, HWANG J H, KIM T G, YIN Ling-hong, LEE H W, KIM J P, AHN H S, CHO C R. Enhanced electrochemical performance of peony flower-like carbon-coated γ-Ga_2O_3 nanosheets for lithium-ion battery anodes [J]. Journal of Ceramic Processing Research, 2021, 22: 192−199.

[45] NAM H G, PARK J Y, YUK J M, HAN S M. Phase transformation mechanism and stress evolution in Sn anode [J]. Energy Storage Materials, 2022, 45: 101−109.

[46] YANG Kai-qi, TANG Ming. Three-dimensional phase evolution and stress-induced non-uniform Li intercalation behavior in lithium iron phosphate [J]. Journal of Materials Chemistry A, 2020, 8: 3060−3070.

[47] LIU Xue-feng, XING Ying-ying, XU Ke, ZHANG Hai-jun, GONG Ming-xing, JIA Quan-li, ZHANG Shao-wei, LEI Wen. Kinetically accelerated lithium storage in high-entropy (LiMgCoNiCuZn)O enabled by oxygen vacancies [J]. Small, 2022, 18: e2200524.

[48] ZHANG Ying-ying, CHEN Peng, WANG Qing-yu, WANG Qian, ZHU Kai, YE Ke, WANG Gui-ling, CAO Dian-xue, YAN Jun, ZHANG Qiang. High-capacity and kinetically accelerated lithium storage in MoO_3 enabled by oxygen vacancies and heterostructure [J]. Advanced Energy Materials, 2021, 11: 2101712.

[49] KE Cheng-zhi, SHAO Rui-wen, ZHANG Ying-gan, SUN

Zhe-fei, QI Shuo, ZHANG He-he, LI Miao, CHEN Zhi-lin, WANG Yang-su, SA Bai-sheng, LIN Hai-chen, LIU Hao-dong, WANG Ming-sheng, CHEN Shuang-qiang, ZHANG Qiao-bao. Synergistic engineering of heterointerface and architecture in new-type ZnS/Sn heterostructures in situ encapsulated in nitrogen-doped carbon toward high-efficient lithium-ion storage [J]. Advanced Functional Materials, 2022, 32: 2205635.

Ga 基液态金属去合金化制备多孔 α-Ga_2O_3 纳米线改善锂存储循环稳定性

罗 畅[1]，王子刚[1]，王宜超[2]，孟帅举[3]，余 晖[1]，赵维民[1]，秦春玲[1]，王志峰[1]

1. 河北工业大学 材料科学与工程学院 河北省“一带一路”先进材料国际联合研究中心，天津 300401；
2. School of Science, RMIT University, Melbourne VIC 3001, Australia;
3. 兰州理工大学 省部共建有色金属先进加工与再利用国家重点实验室，兰州 730050

摘 要：Ga_2O_3 具有较高的理论容量和独特的自愈能力，被认为是下一代锂离子电池的潜在负极材料。为了开发新的制备方法和深入理解 Ga_2O_3 的电化学反应机理，采用一种全新的液−液去合金化策略构建多孔 α-Ga_2O_3 纳米线网络。得益于精心设计的多孔结构，材料表现出优异的循环稳定性，在 1000 mA/g 的电流密度下经过 200 次循环后仍保持 603.9 mA·h/g 的可逆容量。组装成 Ga_2O_3//$LiFePO_4$ 全电池后，在倍率为 0.5*C* 下循环 100 次后可获得 125.2 mA·h/g 的容量保持。通过非原位拉曼光谱、XRD、TEM 测试和密度泛函理论(DFT)计算进一步揭示了多孔 Ga_2O_3 负极的嵌锂/脱锂反应机理，建立了材料的电化学性能与循环过程中 α-Ga_2O_3 向 β-Ga_2O_3 相转变行为的关系。

关键词：液态金属去合金化；多孔纳米线；氧化镓；锂离子电池；负极

(Edited by Wei-ping CHEN)